

Lagged Oceanic Effects on the East African Short Rains

Erik W Kolstad (✉ erikwkolstad@gmail.com)

NORCE Norwegian Research Centre <https://orcid.org/0000-0001-5394-9541>

David MacLeod

University of Bristol

Research Article

Keywords: East Africa, Short rains, Climate prediction, ENSO, Indian Ocean Dipole

Posted Date: September 29th, 2021

DOI: <https://doi.org/10.21203/rs.3.rs-915035/v1>

License:   This work is licensed under a Creative Commons Attribution 4.0 International License.

[Read Full License](#)

1 Lagged oceanic effects on the East African short rains

2 Erik W. Kolstad^{1,2*} and David MacLeod^{3†}

3 ¹ NORCE Norwegian Research Centre, Bjerknes Centre for Climate Research, Bergen, Norway

4 ² Norwegian Meteorological Institute, Bergen, Norway

5 ³ School of Geographical Sciences, University of Bristol, Bristol, UK

6 Abstract

7 The East African ‘short rains’ in October–December (OND) exhibit large interannual variability. Drought
8 and flooding are not unusual, and long-range rainfall forecasts can guide planning and preparedness.
9 Although seasonal forecasts based on dynamical models are making inroads, statistical models based on sea
10 surface temperature (SST) precursors are still widely used. It is important to better understand the sources of
11 skill of statistical models and why they sometimes fail. Here, we define a linear regression model, where the
12 August states of El Niño–Southern Oscillation (ENSO) and the Indian Ocean Dipole (IOD) predict about
13 40% of the short rains variability in 1950–2020. The forecast errors are traced back to the initial SSTs: too-
14 wet (too-dry) forecasts are linked linearly to positive (negative) initial ENSO and IOD states in August. The
15 link to the initial IOD state is mediated by IOD between August and OND, highlighting a physical
16 mechanism for prediction busts. We also identify asymmetry and nonlinearity: when ENSO and/or the
17 IOD are positive in August, the range and variance of OND forecast errors are larger than when the SST
18 indices are negative. Upfront adjustments of predictions conditional on initial SSTs would have helped in
19 some years with large forecast busts, such as the dry 1987 season during a major El Niño, for which the
20 model erroneously predicts copious rainfall, but it would have exacerbated the forecast performance in the
21 wet 2019 season, when the IOD was strongly positive and the model predicts too-dry conditions.

22 **Keywords:** East Africa, Short rains, Climate prediction, ENSO, Indian Ocean Dipole

* E-mail: ekol@norceresearch.no; ORCID: 0000-0001-5394-9541

† ORCID: 0000-0001-5504-6450

23 **Declarations**

24 **Funding:** The research was supported by funding from the European Union’s Horizon 2020 program
25 through the CONFER (grant 869730) and DOWN2EARTH (grant 869550) projects, and from the
26 Research Council of Norway through the Seasonal Forecasting Engine project (grant 270733) and the
27 Climate Futures research centre (grant 309562).

28 **Conflicts of interest/Competing interests:** N/A

29 **Availability of data and material:** The ERA5 data are available from the Copernicus Climate Data Store
30 (Hersbach et al., 2018a, 2018b, 2020a, 2020b).

31 **Code availability:** N/A

32 **Authors’ contributions:** Both authors conceived and wrote the paper, and EWK performed the data analysis
33 and produced the figures and tables.

34 **1 Introduction**

35 Climate variability in East Africa is high, with floods and droughts significantly impacting lives and
36 livelihoods (e.g., Little et al., 2001; Conway et al., 2005; Haile et al., 2019). The ‘short rains’ in the boreal
37 autumn (Dunning et al., 2016; Nicholson, 2017) in particular show substantial interannual variability, with
38 extreme impacts from both flooding (e.g., in 2019; Chang’a et al., 2020; Wainwright et al., 2021) and drought
39 (e.g., in 2010; Dutra et al., 2013).

40 A strong association between El Niño–Southern Oscillation (ENSO) and the short rains has been known
41 for decades (e.g., Ropelewski & Halpert, 1987), and the key importance of the Indian Ocean for the short
42 rains also has a long history (e.g., Nyenzi, 1988; Beltrando & Camberlin, 1993; Hastenrath et al., 1993). The
43 Indian Ocean Dipole (IOD; Saji et al., 1999), which peaks around September–November (e.g., Zheng et al.,
44 2021), is an oceanic driver of the short rains (Latif et al., 1999; Black et al., 2003; Black, 2005; Bahaga et al.,
45 2019), specifically through its role in a local east–west-oriented Walker cell (e.g., Goddard & Graham, 1999;
46 Hastenrath et al., 2004; Behera et al., 2005; Ummenhofer et al., 2009; Nicholson, 2015; Zhao & Cook,
47 2021). Numerous studies have shown that ENSO in boreal summer leads the IOD in boreal autumn (e.g.,
48 Stuecker et al., 2017; McKenna et al., 2020), suggesting a mainly indirect role of ENSO in the context of
49 predicting the short rains. Some studies have estimated the spatial patterns of rainfall anomalies associated
50 with events where both ENSO and the IOD are active, compared to ENSO-only events; the latter showing a
51 weaker and less homogenous rainfall response (MacLeod & Caminade, 2019; MacLeod et al., 2021).

52 Seasonal forecasts can play a central role in planning and preparedness (e.g., Lemos et al., 2012; Bruno
53 Soares et al., 2018; Tall et al., 2018; Bazo et al., 2019; Nyamekye et al., 2021). Forecast skill is underpinned
54 by seasonal predictability arising from teleconnections with large-scale drivers, and with a strong link to ENSO
55 and the IOD, short rains forecasts generally show high levels of skill at long lead times (e.g., Mwangi et al.,
56 2014; MacLeod, 2019). The season is then a prime candidate for forecast-based early actions, and seasonal
57 forecasts have been provided at the Greater Horn of Africa Regional Climate Outlook Forum (GHACOF)
58 meetings for over a decade (Hansen et al., 2011; Walker et al., 2019), with the outlook for October–December
59 (OND) usually produced in late August.

60 The GHACOF forecasts are issued by the Intergovernmental Authority on Development (IGAD) Climate
61 Prediction and Applications Centre (ICPAC) and produced in collaboration with the National Meteorological
62 and Hydrological Services (NMHS) of 11 countries, from Sudan in the north to Tanzania in the south.

63 Previously, the GHACOF forecasts were the outcome of an opaque ‘consensus’ process, which included the
64 use of dynamical forecast models, statistical regression models, and ‘analogue years’ based on the current
65 tropical SST anomalies (mainly ENSO and the IOD). The consensus process has had a ‘tendency to over-
66 forecast the near normal category of rainfall’ (Walker et al., 2019), which is unfortunate because it leads to
67 under-prediction of lower- and upper-tercile events. In an effort to mitigate this problem, the production of
68 the forecasts has gradually evolved towards being based on ‘objective’ dynamical model forecasts in recent
69 years, but there is an understandable reluctance to fully embrace dynamical models.

70 Based on conversations with NMHS representatives, we know that methods based on regressions and
71 analogue years are still widely used in the region. It is therefore important to study the performance of statistical
72 forecast models in predicting the short rains, to learn more about the dynamical pathways linking August SST
73 anomalies and OND rainfall, as well as assessing the years when statistical forecasts fail. This is the purpose of
74 the study described here, which we hope will contribute to a more informed use of statistical models.

75 Specifically, we seek to understand the ability of climate conditions (ENSO and IOD) which are present
76 at the time of the late August GHACOF to anticipate OND rainfall, in order to diagnose those climate states
77 which are (and are not) a useful indication of upcoming climate variability. We do this through the use of a
78 linear regression model based on reanalysis data from 1950 to 2020, relating ENSO and IOD to rainfall and
79 variables that describe the Walker circulation over the Indian Ocean. We then harness the errors of the
80 reanalysis-based linear model as a diagnostic tool, to provide insight into the relationship between August
81 SSTs, the OND Walker circulation, and the short rains. Changes in the SST forcing between the prediction
82 time in August and the OND itself is investigated as a possible source of errors. Furthermore, we study the
83 relationship between OND forecast errors and precursor SST conditions in August to determine if there exist
84 certain conditions which can indicate *a priori* (upfront) the level of uncertainty in a seasonal forecast. We
85 recently used a similar approach to show that the ECMWF monthly forecasting system has a systematic
86 conditional short rains bias contingent on the initial IOD state (Kolstad et al., 2021).

87 Studies of conditional forecast model errors and biases such as the one described herein are relevant for
88 both dynamical forecasts initialised with SST fields which have had notable forecasts busts in recent years
89 (Kilavi et al., 2018; MacLeod & Caminade, 2019), but also for statistical forecasts based on precursor SST
90 conditions. They may also guide the use of analogue forecasts which produce an outlook based on diagnosis
91 of historical seasons with similar SST conditions.

92 **2 Data and methods**

93 **2.1 Data and detrending**

94 ERA5 reanalysis (Hersbach et al., 2020c) monthly mean data from 1950 to 2020 are used throughout.
95 The following variables are analysed: precipitation, SST, vertical velocity at 500 hPa (w_{500} ; positive upwards),
96 and zonal wind at 700 hPa (u_{700}). To compensate for trends during the study period, the SST and
97 precipitation data from ERA5 are linearly detrended. As the data for the other variables have less consistent
98 trends, these are not detrended.

99 **2.2 SST indices**

100 Two SST indices are based on standard regions (e.g., Stuecker et al., 2017): the NINO3.4 index (referred
101 to as N34 from now), calculated as area-averaged SST anomalies from 170°W to 120°W and between 5°S and
102 5°N; and the IOD dipole mode index (DMI hereafter), computed as the difference between area-averaged
103 SST anomalies in the western (50°E to 70°E and 10°S to 10°N) and eastern (90°E to 110°E and 10°S to 0°)
104 Indian Ocean. The detrending was performed after the indices had been computed, and then the N34 and
105 DMI time series were standardized.

106 **2.3 EOF analysis**

107 The rainfall analysis is based on Empirical Orthogonal Functions (EOFs), which reduce vast amounts of
108 data to a limited number of interannual time series. We first calculate detrended ERA5 precipitation OND
109 anomalies for each grid point from 10°S to 12°N and 30°E to 52°E – the same region used by Vigaud et al.
110 (2017) and Kolstad et al. (2021). This gives us 71 precipitation maps, which are used as input to the *eofs*
111 software package for Python (Dawson, 2016). Although not shown here, we also used *k*-means clustering
112 (MacQueen, 1967) to divide the precipitation maps into distinct clusters, and this produced similar patterns
113 to the ones described by the leading EOFs.

114 **2.4 Linear prediction**

115 We predict several variables during OND based on SST indices in August. The choice of August as the
116 initial month is motivated by timing of the GHACOFs addressing the OND season, which are usually held

117 in late August. In addition to predicting the rainfall, we also predict certain variables related to the Walker
 118 circulation, namely SST, w_{500} , and u_{700} , all in OND. Naming the SST indices X_i , where the subscripts 1
 119 and 2 denote N34 and DMI, respectively, we define a regression that describes their lagged relationship with
 120 any variable Y :

$$121 \quad Y = \sum c_i X_i + \rho, \quad (1)$$

122 where ρ is the residual. The non-calibrated prediction of Y is written as:

$$123 \quad \hat{y} = \sum \hat{c}_i X_i. \quad (2)$$

124 We estimate \hat{c}_i separately for each year by using the time series of Y and X_i for all the other years; this
 125 method is usually referred to as ‘out-of-sample’ or ‘leave-one-out’ forecasting. (Note that when predicting the
 126 principal components, we do not compute out-of-sample EOFs for each year, as this might for some years
 127 create different spatial patterns and principal components with opposite signs; we just leave the in-sample
 128 elements of the principal components out.) To scale the prediction, we divide \hat{y} by its out-of-sample standard
 129 deviation and multiply by the out-of-sample standard deviation of Y to obtain a calibrated prediction:

$$130 \quad \hat{Y} = \sigma(Y) \hat{y} / \sigma(\hat{y}). \quad (3)$$

131 2.5 Mediation

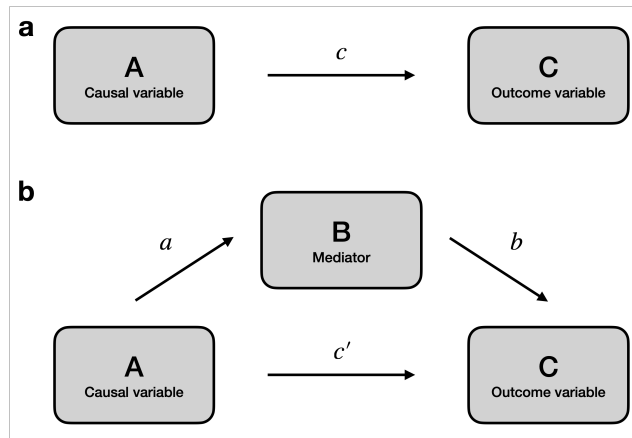
132 If a ‘causal variable’ A is significantly correlated with an ‘outcome variable’ C , we can express this
 133 relationship as $A \rightarrow C$. However, the direct effect of A on C may be mediated by a variable B . This can be
 134 expressed as $A \rightarrow B \rightarrow C$, and the validity of the pathway is checked by going through four ‘steps’ (e.g., Baron
 135 & Kenny, 1986), using regressions illustrated in Fig. 1.

136 First, the coefficient c in Fig. 1a, which describes the direct effect of A on C , must be significant. Otherwise,
 137 there is no effect to be mediated. Second, the coefficient a in Fig. 1b, the direct effect of A on B , must also
 138 be significant to ensure that the mediator is influenced by the causal variable. To check the remaining steps,
 139 we define a linear regression:

$$140 \quad C = c'A + bB, \quad (4)$$

141 Third, b must be significant, which means that B has an effect on C when accounting for A . The fourth
 142 requirement for mediation is that the coefficient c' must be non-significant, as this signifies that the outcome

143 C is conditionally independent of A when accounting for B . If all the four steps are satisfied, the mediator B
144 fully mediates the effect of A on C .



145

146 FIG. 1 (a), A diagram illustrating the direct effect c of the causal variable A on the outcome variable C . (b), A diagram
147 illustrating the direct effect a of A on the mediator B , as well as the regression coefficients of Eq. 4, b and c' .

148 2.6 Significance testing

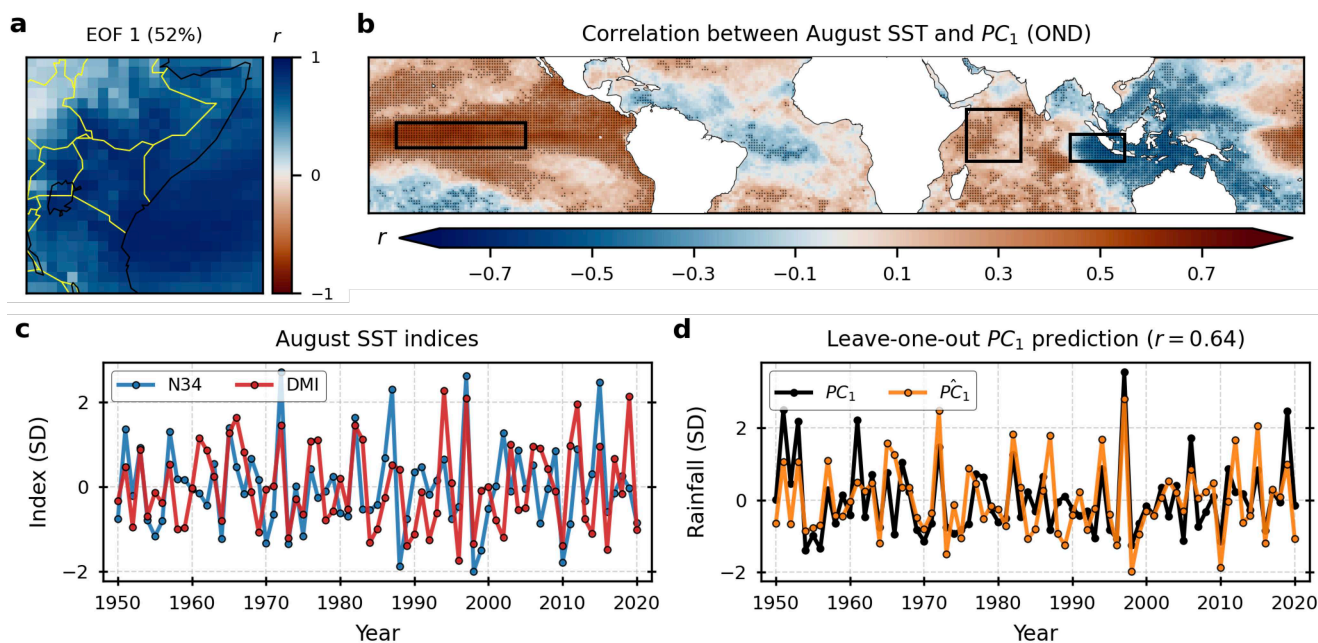
149 Bootstrapping is used to calculate statistical significance. In each case, a set of 1,000 artificial time series is
150 produced by replacing each datum with the datum from a random year between 1950 and 2020 (with
151 replacement). Correlations or regression coefficients are deemed significant at the 5% level (which is used
152 throughout) if they are either less than the 2.5th percentile of the bootstrapped set, or greater than its 97.5th
153 percentile.

154 3. Results

155 3.1 Lagged relationships between SST and rainfall variability

156 In Fig. 2a, the loading patterns of the leading EOF of East African rainfall in OND is shown, expressed as
157 the interannual correlation between the detrended precipitation and PC_1 in each grid point. It describes 52%
158 of the rainfall variance and represents large-scale precipitation anomalies affecting most of the region. This
159 agrees well with first EOF of both Schreck and Semazzi (2004) and Wenhaji Ndomeni et al. (2018), both of
160 whom used other rainfall data sets and reference periods, and slightly different region boundaries. The highest
161 correlations are also in good qualitative agreement with the region with a biannual rainfall regime and

162 October/November onset in Dunning et al. (2016; their Fig. 5d). On the interannual scale, the time series of
 163 the leading principal component (PC_1 hereafter, defined uniquely for OND) is highly correlated with a time
 164 series of area-averaged detrended precipitation anomalies inside the study region, using land points only ($r =$
 165 0.95), confirming that the first EOF represents large-scale rainfall. PC_1 is also significantly correlated with
 166 both N34 ($r = 0.58$) and DMI ($r = 0.73$) in OND.



167

168 FIG. 2 (a) The loading pattern of the leading EOF of East African rainfall, with country borders in yellow. (b)
 169 Interannual correlation between SSTs in August and PC_1 , with significant correlations indicated with dots and the
 170 boundaries of the N34 and IOD regions shown as rectangles. (c) Detrended interannual time series of August N34
 171 and DMI; (d) Time series of PC_1 and its prediction \widehat{PC}_1 .

172 In Fig. 2b, we show the spatial structure of the lagged correlation between tropical SSTs in August and
 173 PC_1 . Inside the NINO3.4 region, the correlations are positive, and the oppositely signed correlations in the
 174 two IOD regions are consistent with a positive lagged correlation with DMI. In index form, PC_1 is
 175 significantly lag-correlated with both N34 ($r = 0.56$) and DMI ($r = 0.55$) in August. There are indications
 176 of significant correlations outside the N34 and DMI regions, such as in the Atlantic, but the two indices
 177 appear to represent a large share of the interannual correlations.

178 Figure 2c shows standardized interannual time series of the detrended August SST indices. The correlation
 179 between the two indices is 0.45. In some years both indices have large values with the same sign, such as during

180 the major El Niño episodes in 1972 and 1997, and the La Niña events in 1998 and 2010. Other years have
 181 large DMI absolute values but weak ENSO conditions, including 2019.

182 The time series for PC_1 is shown in Fig. 2d, along with its (leave-one-out) prediction \widehat{PC}_1 , where Eqs. 1–
 183 3 are used. The Eq. 2 regression coefficients are both significant and similar in magnitude ($\hat{c}_1 = 0.40$ and
 184 $\hat{c}_2 = 0.37$). The correlation between \widehat{PC}_1 and PC_1 is 0.64, and although this may be a slight overestimation
 185 of the actual skill (since the EOFs were not computed out-of-sample; see Sect. 2.4), the high and significant
 186 correlation demonstrates substantial predictive power on the seasonal time scale: about 40% of the interannual
 187 variability of the first principal component of OND rainfall is accounted for by the two SST indices in August,
 188 1–2 months before the rainy season onset.

189 *Table 1. Equation 2 regression coefficients for initial SST indices from June to October. The number in*
 190 *parentheses indicates a non-significant coefficient, and the remaining correlations are significant. The last column*
 191 *shows the correlation between the predicted and actual rainfall index.*

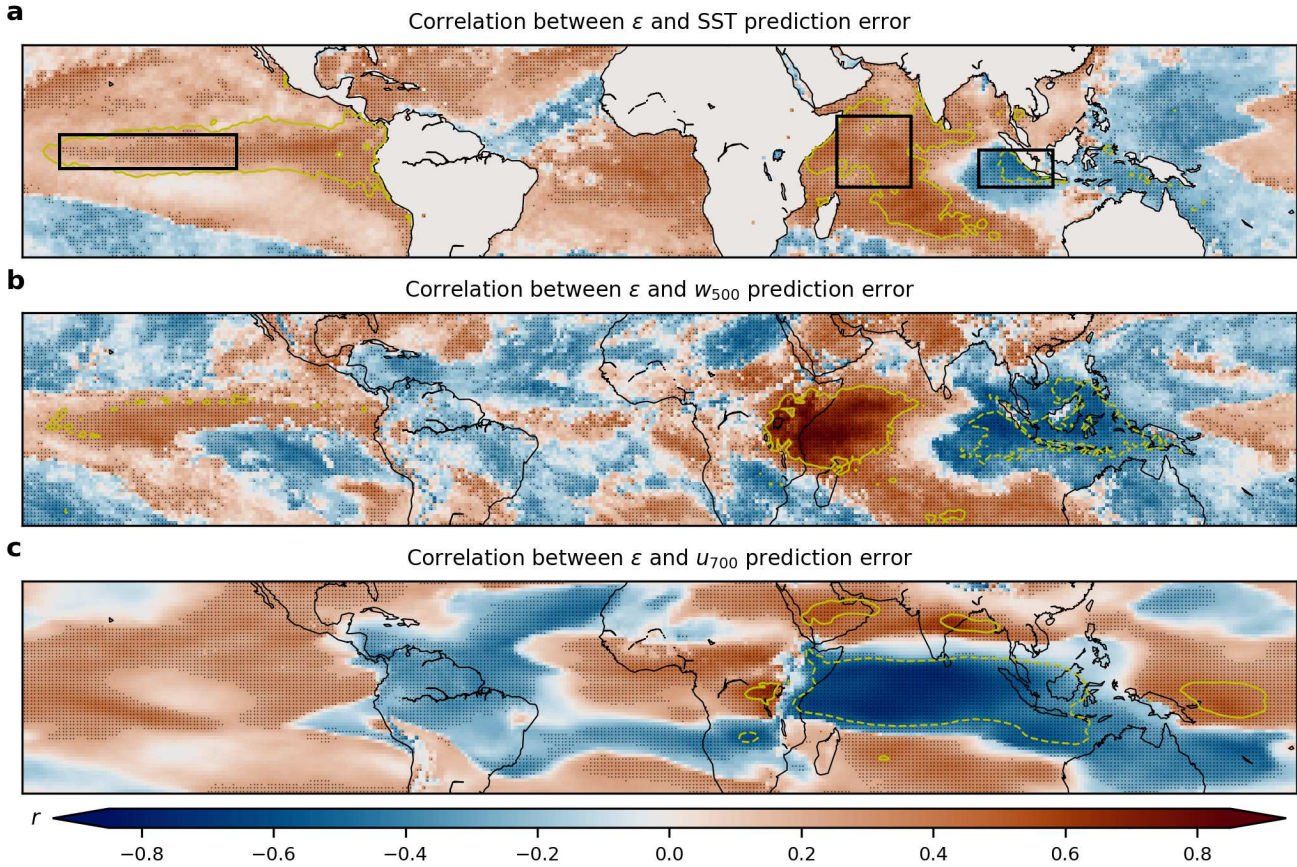
Predictor month	N34 coefficient (\hat{c}_1)	DMI coefficient (\hat{c}_2)	Correlation between \widehat{PC}_1 and PC_1
June	0.29	0.29	0.48
July	0.43	0.30	0.60
August	0.40	0.36	0.64
September	0.30	0.48	0.68
October	(0.16)	0.61	0.71

192 The N34 coefficient \hat{c}_1 is slightly larger than the DMI coefficient \hat{c}_2 , but this changes when the initial
 193 SST state is taken from a different month. Table 1 shows that the relative importance of N34 with respect to
 194 DMI is highest for July initial states, and thereafter it declines (recall that the IOD peaks in September–
 195 November). For October initial states, the N34 coefficient is non-significant, which demonstrates that it is
 196 the IOD that directly influences the East African rainfall at short lags. Furthermore, a mediation analysis of
 197 the effect of August N34 on PC_1 shows that this effect is fully mediated by DMI in OND. Using the notation
 198 in Sect. 2.5, we let the causal variable A be N34 in August, the mediator B is DMI in OND, and the outcome
 199 C is PC_1 , and then we go through the four steps required for mediation sequentially. First, as mentioned
 200 earlier, c is significant (the correlation between August N34 and PC_1 is 0.56). Second, the coefficient a is also
 201 significant with a value of 0.65, representing the ENSO-leading-IOD relationship (Stuecker et al., 2017).
 202 Third, the coefficient b in Eq. 4 is significant with a value of 0.63. Fourth, the coefficient c' is non-significant,
 203 which shows that PC_1 is independent of August N34 given DMI in OND.

204 3.2 Dynamical pathways

205 We now investigate PC_1 and its prediction \widehat{PC}_1 in more detail. Our main purpose is not to validate the
206 prediction model, but rather to use that model to better understand the dynamical linkages between August
207 SSTs and large-scale OND rainfall. Our approach is to investigate when and why the linear model fails: when
208 \widehat{PC}_1 deviates from PC_1 . There are linear aspects to these failures, but we are also interested in nonlinear aspects,
209 and especially large deviations between \widehat{PC}_1 and PC_1 . For brevity, we refer to the forecast error as $\varepsilon \stackrel{\text{def}}{=} \widehat{PC}_1 -$
210 PC_1 .

211 Before we study the forecast errors, we assess how PC_1 relates to concurrent anomalies of SST, w_{500} , and
212 u_{700} (Fig. 3, yellow contours). Figure 3a shows that rainfall and SST anomalies are positively correlated in the
213 western part of the Indian Ocean, and negatively correlated in the eastern part. This is consistent with the
214 positive correlation between DMI and East African rainfall. The positive correlations in the eastern Pacific,
215 including in the NINO3.4 region, are probably mainly due to teleconnections with the IOD region (see
216 Section 3.1). For the vertical velocity, a large area over the western Indian Ocean and East Africa has high
217 positive correlations with PC_1 , with negative correlations in evidence over the eastern Indian Ocean (Fig. 3b).
218 In Fig. 3c, the low-level zonal wind is shown to be negatively correlated with PC_1 over the whole central
219 Indian Ocean. In sum, the correlations over the Indian Ocean in the three panels of Fig. 3 are all consistent
220 with a positive IOD state and an enhanced Walker circulation during periods with higher-than-normal
221 rainfall, and a negative IOD state and a suppressed Walker circulation during drier-than-normal periods. This
222 is not a new result, but the correlations in yellow in Fig. 3 are a useful reference for the next part of the analysis.



223

224

225

226

227

228

229

230

231

232

233

234

235

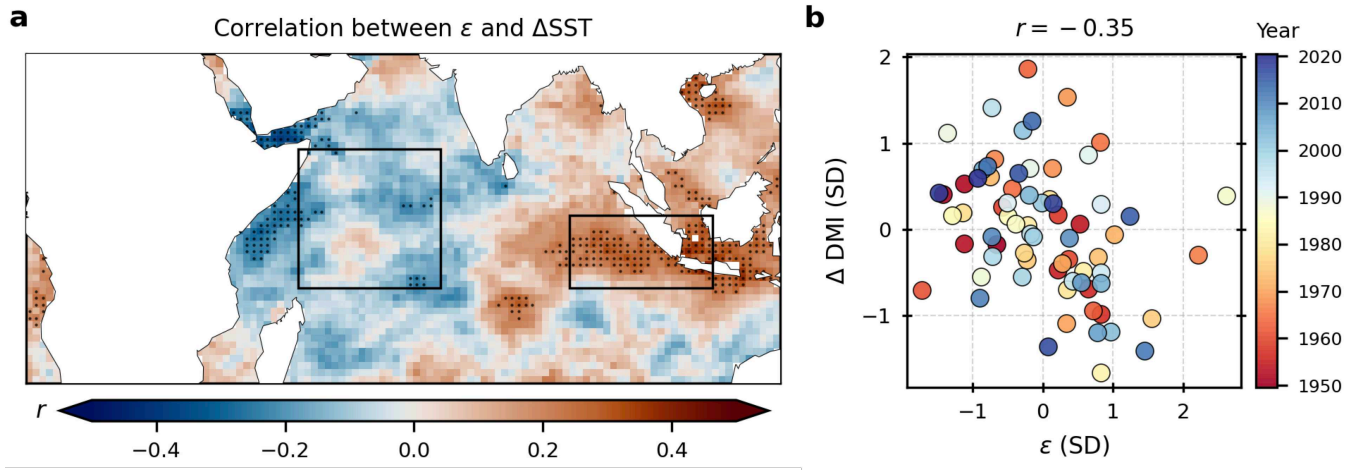
236

FIG. 3 Interannual correlation between ε and the OND prediction error of the following variables: SST (a); 500-hPa vertical velocity (b); and 700-hPa zonal wind (c). Significant correlations are indicated with dots, and the yellow contours show the +0.5 (solid) and -0.5 (dashed) isolines for the correlation between PC_1 and OND anomalies of each variable. In (a), the boundaries of the IOD and ENSO regions are shown as rectangles.

We now use Eqs. 1–3 to predict SST, vertical velocity, and zonal wind in OND, based on the two SST indices in August, just as we predicted PC_1 . This is done for all grid points individually, and then we compute the correlation between the forecast errors $\hat{Y} - Y$ and ε , where Y is SST, w_{500} , and u_{700} , in turn. These correlations are shown with colours in Fig. 3. Over the Indian Ocean, there is good correspondence between the forecast error correlations and the correlations shown in yellow. When too much rainfall is predicted, too-positive SST anomalies are predicted in the western Indian Ocean (Fig. 3a), with too-positive overlying w_{500} anomalies (Fig. 3b), and too-negative u_{700} anomalies are predicted over the Indian Ocean (Fig. 3c). In the eastern part of the Indian Ocean, too-negative SST anomalies and too-negative w_{500} anomalies complete the Walker circulation signature.

237 In other words, when the linear East African rainfall prediction model fails, similar linear models fail to
 238 predict SST, vertical velocity, and low-level zonal wind anomalies in the areas where said variables are
 239 correlated with East African rainfall. One interpretation of this finding is that the SST indices in August
 240 usually predict the Walker circulation in OND quite well, and hence also East African rainfall, but when the
 241 Walker circulation deviates from the expected ‘response’ to the August SSTs, the OND rainfall prediction
 242 fails. What could drive an unexpected OND Walker circulation response to August SSTs and hence an error
 243 in the rainfall prediction based on August SST indices? One possibility, which we investigate in the next
 244 section, is that the SSTs in the Indian Ocean evolve substantially between August and OND, which again
 245 might lead to different SST forcing to the one predicted by the linear model.

246 **3.3 Role of SST changes**



247
 248 FIG. 4 (a) Interannual correlation between Δ SST and ϵ . Significant correlations are indicated with dots, and the
 249 rectangles indicate the outlines of the IOD regions. (b) Scatterplot of ϵ on the x-axis versus Δ DMI on the y-axis (both
 250 in standard deviations). The colours of the circles correspond to the years.

251 The map in Fig. 4a shows the correlation between ϵ and Δ SST (the change in SST from August to OND)
 252 in the Indian Ocean (the changes in the N34 region are non-significant and therefore not shown). The general
 253 pattern is that when too much rainfall is predicted, the western part of the Indian Ocean cools and the eastern
 254 part warms. This pattern is compatible with a de-intensification of the Walker circulation, which again is
 255 consistent with a decrease in the East African rainfall. In other words, if the IOD index decreases between
 256 August and OND, the actual rainfall tends to be less than what the model predicts. Conversely, when the

257 prediction is too dry, the Walker circulation intensifies due to SST warming in the west and cooling in the
258 east, and the actual rainfall is greater than the predicted rainfall.

259 Although the significant blue areas in Fig. 4a in the western Indian Ocean are concentrated to the west of
260 the western IOD region, there is clearly a negative correlation between changes in DMI and the rainfall forecast
261 error. In Fig. 4b, ΔDMI (the change in DMI from August to OND) is plotted against ε for each year. The
262 correlation is -0.35 , which is statistically significant. In all the years where DMI decreases by more than one
263 standard deviation, the rainfall forecast error is positive. However, there are years with large positive forecast
264 errors where DMI does not decrease notably. In the El Niño year of 1987 (see Fig. 2c), the largest positive ε
265 value is found, but DMI in fact increased slightly between August and OND. We also note that large positive
266 ΔDMI values are not uniformly linked to negative rainfall forecast errors. For instance, the year with the
267 second-largest DMI increase (1969), ε is positive.

268 In sum, the correlation of -0.35 (Fig. 4b) shows that about 10% of the rainfall forecast error can be linked
269 linearly to DMI changes. However, it is not generally possible to know in advance how SSTs will change
270 between August and OND. It would be more useful if we could identify a relationship between the initial
271 state in August and the subsequent prediction errors in OND, as these could potentially make it possible to
272 foresee *a priori* whether the linear model is more likely to fail.

273 3.4 Role of initial SSTs

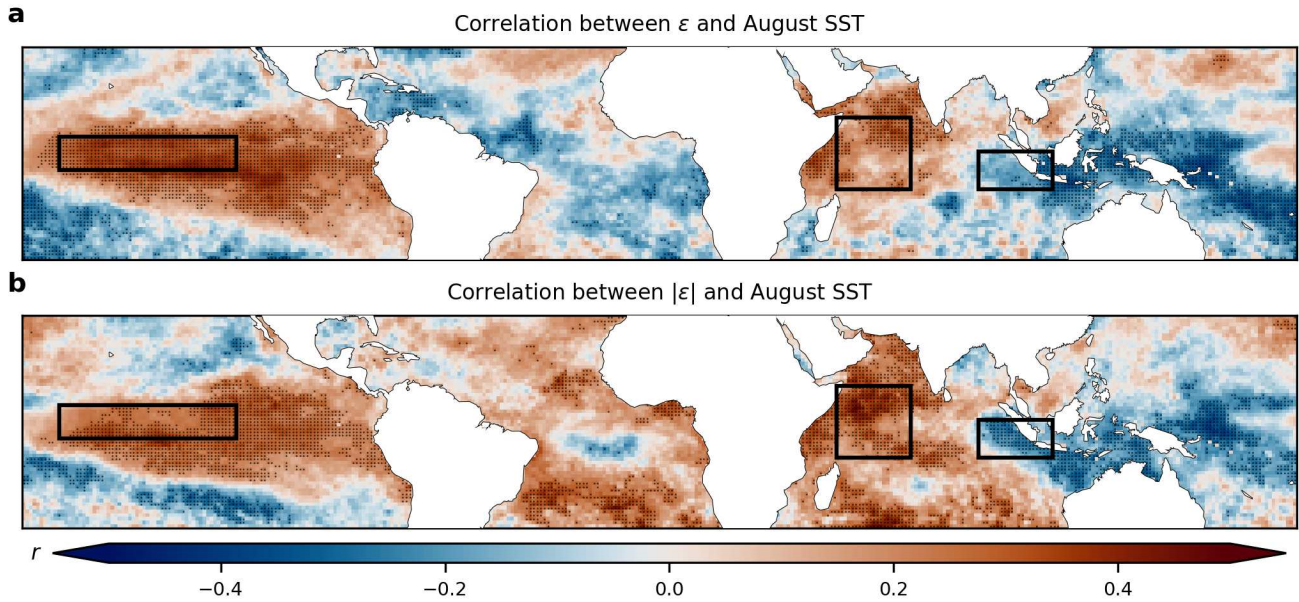
274 First, to get a qualitative overview of the most severe prediction busts, we study the seven years (roughly
275 10% of the 71 years in the study period) with the largest negative errors, as well as the seven years with the
276 largest positive errors, i.e., when the model is too dry and too wet, respectively. For these years, PC_1 , its
277 prediction \widehat{PC}_1 , the error ε , and the August SST indices are listed in Table 2.

278 For some of the years, the errors are large because \widehat{PC}_1 has the wrong sign, such as in 1952, for which the
279 model predicts drier-than-average conditions ($\widehat{PC}_1 = -0.7$) but the actual rainfall was wetter than average
280 ($PC_1 = 0.5$). In the El Niño year of 1987, the model predicts heavy rain ($\widehat{PC}_1 = 1.8$), but in reality, the
281 conditions were drier than normal ($PC_1 = -0.8$). In other cases, \widehat{PC}_1 has the right sign, but the magnitude
282 is incorrect, such as in 2019, when the IOD was strongly positive, for which $\widehat{PC}_1 = 1.0$, but the actual rainfall
283 was extremely high (Wainwright et al., 2021): $P = 2.5$.

284 Table 2. The seven years in each category (too-dry and too-wet), ranked by the rainfall forecast error magnitude.
 285 The unit is standard deviations. Note that rounding errors leads to some apparently inconsistent ε values.

Too-dry forecasts						Too-wet forecasts					
Year	ε	PC_1	\widehat{PC}_1	August N34	August DMI	Year	ε	PC_1	\widehat{PC}_1	August N34	August DMI
1961	-1.7	2.2	0.5	-0.1	1.2	1987	2.6	-0.8	1.8	2.3	0.5
2019	-1.5	2.5	1.0	-0.0	2.1	1966	2.2	-1.0	1.3	0.5	1.6
1951	-1.4	2.5	1.1	1.4	0.5	1976	1.6	-0.7	0.9	0.4	1.1
1989	-1.4	0.1	-1.3	-0.8	-1.4	2012	1.4	0.2	1.7	0.9	2.0
1984	-1.3	0.2	-1.1	-0.5	-1.3	2015	1.2	0.8	2.1	2.5	1.0
1978	-1.1	0.6	-0.5	-0.1	-0.8	1972	1.0	1.5	2.5	2.7	1.5
1952	-1.1	0.5	-0.7	-0.2	-1.0	2003	1.0	-0.4	0.5	-0.1	1.0
Average	-1.4	1.2	-0.1	-0.1	-0.1	Average	1.6	-0.1	1.5	1.3	1.2

286 The too-dry cases shown in Table 2 have no consistent August N34 and DMI sign; across the seven years
 287 the average state is neutral for both SST indices. Correspondingly the rainfall prediction \widehat{PC}_1 is also near-zero
 288 on average, whilst observed rainfall is positive in all years, with a strongly positive average PC_1 value (1.3).
 289 The situation is different for the seven too-wet cases. Here there is a consistent sign in August N34 and DMI
 290 values: positive in nearly all cases and strongly positive on average. The average rainfall prediction \widehat{PC}_1 in these
 291 too-wet years is strongly positive (1.5), as expected from the SST indices, but there is no consistent sign in the
 292 observed rainfall indices wet forecasts, showing a near-zero average PC_1 value of -0.1 .



293

294

295

FIG. 5 Maps: Interannual correlation between SST anomalies in August and ε (a) and its magnitude, $|\varepsilon|$ (b). Significant correlations are indicated with dots, and the boxes indicate the outlines of the N34 and IOD regions.

296

297

298

299

300

301

302

303

We now return to all 71 years to fully evaluate the link between August SST state and rainfall prediction error. In Fig. 5a, the correlation between August SST anomalies and ε is shown. This shows a clear linear relationship between ε and both ENSO and the IOD, with positive phases of the SST indices in August tending to result more often in too-wet rainfall predictions, and negative phases tending to result in too-dry predictions. We quantify this with a correlation between ε and the indices, resulting in 0.36 and 0.34 for N34 and DMI, respectively. This is an important result, but the last row of Table 2 shows that, for the most extreme cases, there is an asymmetry in that the too-wet predictions are linked to positive initial ENSO and IOD states, but the too-dry cases are not linked to negative initial ENSO and IOD conditions.

304

305

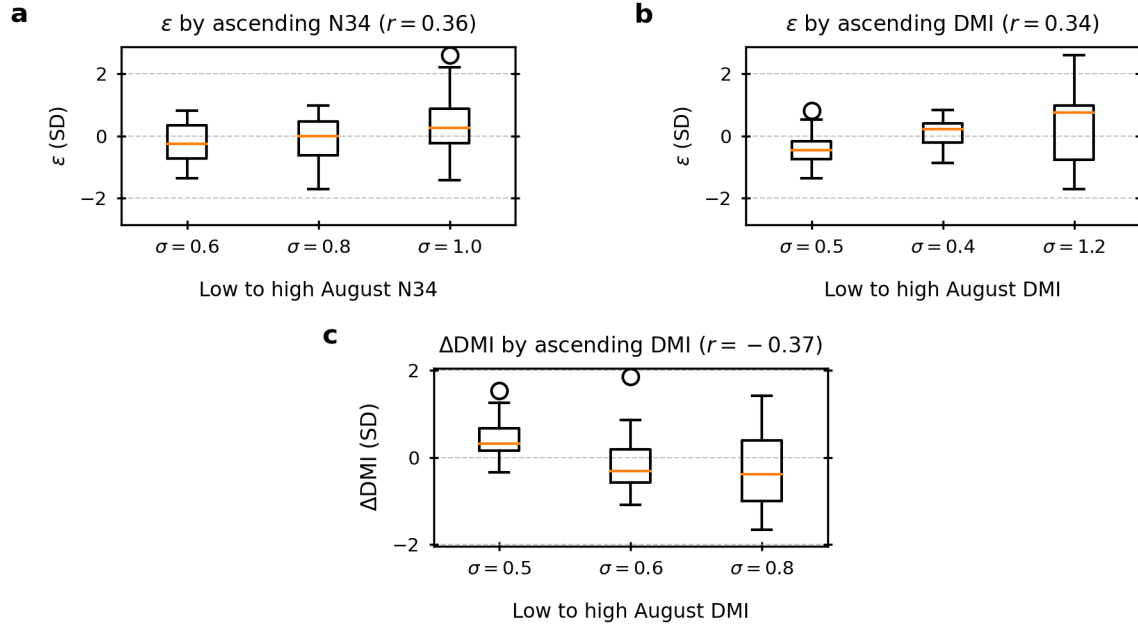
306

307

308

309

This asymmetry points to a nonlinear aspect to the relationship between the initial oceanic state and ε , and we examine this potential link in Fig. 5b by showing the correlation between $|\varepsilon|$ and August SST anomalies for all the 71 years. Clearly, both negative and positive rainfall prediction errors are correlated with both ENSO and the IOD in August. In particular, we note that the SSTs in both IOD regions show a stronger correlation with $|\varepsilon|$ than with ε (Fig. 5a). We now investigate these asymmetric relationships further by dividing the 71 years into three bins, organized by ascending initial N34 and DMI index values, in turn.



310

311 FIG. 6 Top row: Box plots of the distribution of ε , sorted into bins according to August N34 (a) and DMI (b) values
 312 (increasing from left to right). Each rectangle extends from the lower (Q1) to the upper quartile (Q3) of ε , and the
 313 horizontal lines show the median. The upper ‘whiskers’ extend to the highest data points lower than $Q3 + 1.5 \text{ IQR}$,
 314 where the interquartile range $\text{IQR} = Q3 - Q1$, and the lower whiskers extend to the lowest data points greater than
 315 $Q1 - 1.5 \text{ IQR}$. The standard deviation of ε in each bin is indicated along the x-axes, and outliers are shown with
 316 circles. (c), Δ DMI by ascending August DMI values, with conventions as in the two preceding panels.

317 The top row of Fig. 6 shows boxplots (e.g., Krzywinski & Altman, 2014) representing the distribution of
 318 the forecast error ε in each bin. We first note that the median of each bin increases from left to right, reflecting
 319 the positive linear relationship between ε and the August SST indices seen in Fig. 5a. For the N34 index in
 320 Fig. 6a, we see that the standard deviation of the errors is lowest in the first bin, where the N34 index is
 321 negative. In the third bin, where N34 is positive, the range of the errors is largest, and the lowermost whisker
 322 of the rightmost bin extends as far into negative territory as the lowermost whisker of the leftmost bin. Similar
 323 behaviour is seen for DMI in Fig. 6b, but the standard deviation of the third bin is more than twice as large
 324 as the standard deviation of the first bin.

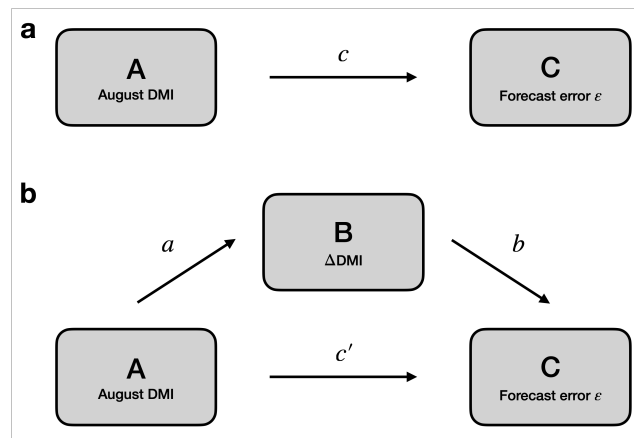
325 In sum, the boxplots in the top row of Fig. 6 illustrate the nonlinear relationship between the initial SST
 326 indices and the rainfall forecast error ε . When the SST indices are positive in August, the error of the linear
 327 prediction model is less predictable and spans a larger interval than when the SST indices are neutral or
 328 negative (see also Fig. 5b), making ε difficult to predict *a priori*.

329 Figure 6c shows that ΔDMI is also both linearly and nonlinearly associated with August DMI values. The
 330 correlation between August DMI and ΔDMI is significant and negative (-0.37), which implies that, on
 331 average, DMI regresses toward the mean between August and OND. The nonlinearity of the relationship is
 332 clear: the standard deviation of ΔDMI in the bin with the highest August DMI values is almost twice as high
 333 as the standard deviation in the bin with the lowest initial values.

334 3.5 Mediating role of DMI changes

335 In the preceding sections, we have shown that both the rainfall forecast error ε and ΔDMI are correlated
 336 with August DMI values. We now use the mediation analysis framework in Sect. 2.5 to assess whether ΔDMI
 337 mediates the lagged effect of August DMI on ε . (Note that as there is no significant effect of ΔN34 on ε ,
 338 ΔN34 is not a potential mediator.) In Fig. 7, we have updated Fig. 1 with the names of the causal variable A
 339 (DMI in August), the potential mediator B (ΔDMI), and the outcome variable C (ε).

340



341 FIG. 7 (a), A diagram illustrating the direct effect c of the causal variable A (August DMI) on the outcome variable C
 342 (ε). (b), A diagram illustrating the direct effect a of A on the mediator B (ΔDMI), as well as the regression coefficients
 343 of Eq. 4, b and c' .

344 We now go through the four steps required for mediation. First, we already know from the previous section
 345 (see Fig. 6b) that the correlation coefficient c in Fig. 7a is significant. Second, the previous section also showed
 346 that correlation coefficient a in Fig. 7b is significant. Using Eq. 4, we can calculate the coefficients b and c' ,
 347 which are -0.30 and 0.21 , respectively. Bootstrapping shows that b is significant, but c' is non-significant
 348 (although its value is very close to the 2.5th percentile of the bootstrapped set of artificial c' coefficients). This

349 means that all the four steps in the mediation check are satisfied, and we have shown that ΔDMI mediates the
350 lagged effect of August DMI on ε . Note that even if c' had been significant, its value is considerably smaller
351 than the coefficient c ($c'/c = 0.61$). Cases for which the first three steps are satisfied, but where c' is significant
352 but $|c'/c| < 1$, are often referred to as ‘partial mediation’.

353 4. Summary and Discussion

354 We have studied the lagged relationship between tropical SSTs in August and the East African short rains
355 from October to December. By working with detrended ERA5 reanalysis data from 1950 to 2020, we obtained
356 the following main results, which are discussed further here:

357 1. A linear prediction model based on the ENSO and IOD states in August accounts for about 40% of
358 the interannual variance of an East African rainfall index, which again accounts for more than half of the
359 spatial and temporal rainfall variance in the region. Although the N34 index in August is a significant predictor
360 of OND rainfall, we showed that this direct effect is fully mediated by the IOD index DMI in OND. The
361 high prediction skill of the linear model is consistent with previous research and here we confirm the result
362 for a long 70-year record. Since linear regression models are still widely used in East Africa it is important to
363 know why and when such models fail. For this reason, the remaining analysis uses this linear model, and
364 particularly its errors, to study the dynamical linkages across time and space between August SSTs and OND
365 rainfall, as well as to assess whether it is possible to predict the forecast errors *a priori*, based on the initial
366 SSTs.

367 2. Tropical SSTs in August are linked to the East African short rains in OND through a Walker circulation
368 across the Indian Ocean. We investigated the correlations between the linear rainfall prediction errors and
369 errors of similarly defined linear prediction models for vertical velocities, low-level zonal winds, and tropical
370 SSTs. The rationale for this approach is that areas where the error correlations are positive pinpoint areas
371 where the other variables ‘communicate’ the lagged effects of the SSTs on the rainfall. When too-much rainfall
372 is predicted, too-positive upwards vertical velocity is also predicted over the western Indian Ocean. Too-high
373 rainfall predictions are also correlated with too-negative zonal wind components over the central Indian Ocean
374 and too-high SSTs in the western part of the basin.

375 3. Rainfall forecast errors are linked to changes in Indian Ocean SSTs between August and OND. On
376 average, negative DMI changes – cooling in the western and warming in the eastern parts of the basin – are

377 associated with positive rainfall prediction errors. In other words, the model predicts too much rain because
378 DMI and the Walker circulation are weaker in OND than they are predicted to be based on the state in
379 August. Conversely, too little rain is predicted in the opposite case when the Walker circulation intensifies
380 between August and OND. However, there are several exceptions to this ‘rule’, and the DMI changes only
381 account for just over 10% of the prediction errors.

382 4. Rainfall forecast errors in OND are also linked across time with the oceanic state in August. The sign
383 of the ENSO and IOD conditions in August is correlated with the sign of the subsequent prediction error.
384 This can potentially be exploited by correcting the predictions upfront. For example, when DMI and N34 are
385 positive in August and the linear model predicts higher-than-average rainfall, the prediction might be adjusted
386 downwards *a priori*. Referring to the list of too-wet forecasts in Table 2, such an approach would have worked
387 in 1987, when the linear model predicts abundant rainfall, but in reality, the conditions were drier-than-
388 normal. It would also have worked in the high-DMI years 1966, 1976, and 2012, and it would have worked
389 in 1972 and 2015, when both N34 and DMI were strongly positive. However, the approach would only have
390 been successful for four of the seven years with the largest negative rainfall prediction errors, when the
391 predicted rainfall might have been adjusted upwards. Notably, the approach would not have worked in 2019,
392 when the region experienced flooding (Wainwright et al., 2021) but for which the model predicts too little
393 rain.

394 5. The relationship between OND rainfall forecast errors and the August SST conditions also have
395 nonlinear aspects. By separating the 71 years into three bins according to August N34 and DMI, we showed
396 that the bin with the highest initial index values has substantially larger error variability than the bin with the
397 lowest initial values. A practical implication is that an *a priori* adjustment of the forecast is less reliable when
398 the ENSO and/or the IOD are in the positive phase in August. The 2019 season is a prime example. In
399 August, DMI in August was 2.1 standard deviations, and as the model prediction for 2019 is already too dry,
400 a further upfront downward adjustment of the prediction based on the positive IOD state would have
401 exacerbated the forecast error. Examples such as this are an argument for using coupled dynamical models,
402 which one can hope are or will be able to capture non-linear evolutions of SSTs and Walker circulations in
403 and over the Indian Ocean.

404 6. Despite the nonlinear nature of the lagged relationships between August SSTs and short rains prediction
405 errors, we identified a mechanism which mediates the lagged linear effect of the IOD state in August on these

406 errors, namely changes in DMI between August and OND. The causal pathway is as follows. The DMI in
407 August has a direct effect on its own subsequent evolution. Positive and negative August values both tend to
408 regress toward the mean. This means that the strength of the Walker circulation in OND can differ from what
409 is expected by the prediction model in August, which again leads to erroneous short rains predictions.

410 In summary, this study has shown that statistical short rains forecasts based on the IOD and ENSO states
411 in August is quite skilful. However, the linear prediction model has a systematic bias which is conditional, in
412 both a linear and a nonlinear sense, on the initial state. In some cases, an *a priori* adjustment of the forecast
413 can lead to improved forecasts, but the nonlinear characteristic of the forecast bias makes such adjustments
414 perilous, especially when the initial IOD state is positive. These results highlight knowledge gaps around the
415 relationships between the East African short rains and the large-scale drivers which underlie the high
416 predictability of this season.

417 Acknowledgements

418 References

- 419 Bahaga, T. K., Fink, A. H., & Knippertz, P. (2019). Revisiting interannual to decadal teleconnections influencing seasonal rainfall
420 in the Greater Horn of Africa during the 20th century. *International Journal of Climatology*, 39(5), 2765-2785.
421 <https://doi.org/10.1002/joc.5986>
- 422 Baron, R. M., & Kenny, D. A. (1986). The moderator–mediator variable distinction in social psychological research: Conceptual,
423 strategic, and statistical considerations. *Journal of Personality and Social Psychology*, 51(6), 1173–1182.
424 <https://doi.org/10.1037/0022-3514.51.6.1173>
- 425 Bazo, J., Singh, R., Destrooper, M., & Coughlan de Perez, E. (2019). Chapter 18 - Pilot Experiences in Using Seamless Forecasts
426 for Early Action: The “Ready-Set-Go!” Approach in the Red Cross. In A. W. Robertson & F. Vitart (Eds.), *Sub-Seasonal
427 to Seasonal Prediction* (pp. 387-398): Elsevier.
- 428 Behera, S. K., Luo, J.-J., Masson, S., Delecluse, P., Gualdi, S., Navarra, A., & Yamagata, T. (2005). Paramount Impact of the
429 Indian Ocean Dipole on the East African Short Rains: A CGCM Study. *Journal of Climate*, 18(21), 4514-4530.
430 <https://doi.org/10.1175/jcli3541.1>
- 431 Beltrando, G., & Camberlin, P. (1993). Interannual variability of rainfall in the eastern horn of Africa and indicators of
432 atmospheric circulation. *International Journal of Climatology*, 13(5), 533-546.
433 <https://doi.org/https://doi.org/10.1002/joc.3370130505>
- 434 Black, E. (2005). The relationship between Indian Ocean sea–surface temperature and East African rainfall. *Philosophical
435 Transactions of the Royal Society A: Mathematical, Physical and Engineering Sciences*, 363(1826), 43-47.
436 <https://doi.org/10.1098/rsta.2004.1474>
- 437 Black, E., Slingo, J., & Sperber, K. R. (2003). An Observational Study of the Relationship between Excessively Strong Short
438 Rains in Coastal East Africa and Indian Ocean SST. *Monthly Weather Review*, 131(1), 74-94.
439 [https://doi.org/10.1175/1520-0493\(2003\)131<0074:Aosotr>2.0.Co;2](https://doi.org/10.1175/1520-0493(2003)131<0074:Aosotr>2.0.Co;2)
- 440 Bruno Soares, M., Daly, M., & Dessai, S. (2018). Assessing the value of seasonal climate forecasts for decision-making. *Wiley
441 Interdisciplinary Reviews: Climate Change*, 9(4), e523. <https://doi.org/10.1002/wcc.523>
- 442 Chang’a, L. B., Kijazi, A. L., Mafuru, K. B., Kondowe, A. L., Osima, S. E., Mtongori, H. I., . . . Michael, E. (2020). Assessment
443 of the evolution and socio-economic impacts of extreme rainfall events in October 2019 over the east Africa. *Atmospheric
444 and Climate Sciences*, 10(3), 319-338. <https://doi.org/10.4236/acs.2020.103018>

445 Conway, D., Allison, E., Felstead, R., & Goulden, M. (2005). Rainfall variability in East Africa: implications for natural resources
446 management and livelihoods. *Philosophical Transactions of the Royal Society A: Mathematical, Physical and Engineering*
447 *Sciences*, 363(1826), 49-54. <https://doi.org/doi:10.1098/rsta.2004.1475>

448 Dunning, C. M., Black, E. C. L., & Allan, R. P. (2016). The onset and cessation of seasonal rainfall over Africa. *Journal of*
449 *Geophysical Research: Atmospheres*, 121(19), 11,405-411,424. <https://doi.org/https://doi.org/10.1002/2016JD025428>

450 Dutra, E., Magnusson, L., Wetterhall, F., Cloke, H. L., Balsamo, G., Bousssetta, S., & Pappenberger, F. (2013). The 2010–2011
451 drought in the Horn of Africa in ECMWF reanalysis and seasonal forecast products. *International Journal of Climatology*,
452 33(7), 1720-1729. <https://doi.org/https://doi.org/10.1002/joc.3545>

453 Goddard, L., & Graham, N. E. (1999). Importance of the Indian Ocean for simulating rainfall anomalies over eastern and
454 southern Africa. *Journal of Geophysical Research: Atmospheres*, 104(D16), 19099-19116.
455 <https://doi.org/https://doi.org/10.1029/1999JD900326>

456 Haile, G. G., Tang, Q., Sun, S., Huang, Z., Zhang, X., & Liu, X. (2019). Droughts in East Africa: Causes, impacts and resilience.
457 *Earth-Science Reviews*, 193, 146-161. <https://doi.org/https://doi.org/10.1016/j.earscirev.2019.04.015>

458 Hansen, J. W., Mason, S. J., Sun, L., & Tall, A. (2011). Review Of Seasonal Climate Forecasting For Agriculture In Sub-Saharan
459 Africa. *Experimental Agriculture*, 47(2), 205-240. <https://doi.org/10.1017/S0014479710000876>

460 Hastenrath, S., Nicklis, A., & Greischar, L. (1993). Atmospheric-hydrospheric mechanisms of climate anomalies in the western
461 equatorial Indian Ocean. *Journal of Geophysical Research: Oceans*, 98(C11), 20219-20235.
462 <https://doi.org/https://doi.org/10.1029/93JC02330>

463 Hastenrath, S., Polzin, D., & Camberlin, P. (2004). Exploring the predictability of the ‘Short Rains’ at the coast of East Africa.
464 *International Journal of Climatology*, 24(11), 1333-1343. <https://doi.org/https://doi.org/10.1002/joc.1070>

465 Hersbach, H., Bell, B., Berrisford, P., Biavati, G., Horányi, A., Muñoz Sabater, J., . . . Thépaut, J.-N. (2018a). *ERA5 monthly*
466 *averaged data on pressure levels from 1979 to present*. <https://doi.org/10.24381/cds.6860a573>

467 Hersbach, H., Bell, B., Berrisford, P., Biavati, G., Horányi, A., Muñoz Sabater, J., . . . Thépaut, J.-N. (2018b). *ERA5 monthly*
468 *averaged data on single levels from 1979 to present*. <https://doi.org/10.24381/cds.f17050d7>

469 Hersbach, H., Bell, B., Berrisford, P., Biavati, G., Horányi, A., Muñoz Sabater, J., . . . Thépaut, J.-N. (2020a). *ERA5 monthly*
470 *averaged data on pressure levels from 1950 to 1978 (preliminary version)*.

471 Hersbach, H., Bell, B., Berrisford, P., Biavati, G., Horányi, A., Muñoz Sabater, J., . . . Thépaut, J.-N. (2020b). *ERA5 monthly*
472 *averaged data on single levels from 1950 to 1978 (preliminary version)*.

473 Hersbach, H., Bell, B., Berrisford, P., Hirahara, S., Horányi, A., Muñoz-Sabater, J., . . . Thépaut, J.-N. (2020c). The ERA5
474 global reanalysis. *Quarterly Journal of the Royal Meteorological Society*, 146(730), 1999–2049.
475 <https://doi.org/10.1002/qj.3803>

476 Kilavi, M., MacLeod, D., Ambani, M., Robbins, J., Dankers, R., Graham, R., . . . Todd, M. C. (2018). Extreme Rainfall and
477 Flooding over Central Kenya Including Nairobi City during the Long-Rains Season 2018: Causes, Predictability, and
478 Potential for Early Warning and Actions. *Atmosphere*, 9(12), 472. <https://doi.org/10.3390/atmos9120472>

479 Kolstad, E. W., MacLeod, D., & Demissie, T. D. (2021). Drivers of subseasonal rainfall forecast errors over East Africa.
480 *Geophysical Research Letters*. <https://doi.org/10.1029/2021GL093292>

481 Krzywinski, M., & Altman, N. (2014). Visualizing samples with box plots. *Nature Methods*, 11(2), 119-120.
482 <https://doi.org/10.1038/nmeth.2813>

483 Latif, M., Dommenges, D., Dima, M., & Grötzner, A. (1999). The role of Indian Ocean sea surface temperature in forcing East
484 African rainfall anomalies during December–January 1997/98. *Journal of Climate*, 12(12), 3497-3504.
485 [https://doi.org/10.1175/1520-0442\(1999\)012<3497:TROIOS>2.0.CO;2](https://doi.org/10.1175/1520-0442(1999)012<3497:TROIOS>2.0.CO;2)

486 Lemos, M. C., Kirchhoff, C. J., & Ramprasad, V. (2012). Narrowing the climate information usability gap. *Nature Clim. Change*,
487 2(11), 789-794. <https://doi.org/10.1038/nclimate1614>

488 Little, P. D., Mahmoud, H., & Coppock, D. L. (2001). When deserts flood: risk management and climatic processes among East
489 African pastoralists. *Climate Research*, 19(2), 149-159. <https://doi.org/10.3354/cr019149>

490 MacLeod, D. (2019). *Seasonal forecast skill over the Greater Horn of Africa: a verification atlas of System 4 and SEAS5 - part1/2*.
491 ECMWF. Retrieved from <https://www.ecmwf.int/node/18906>

492 MacLeod, D., & Caminade, C. (2019). The moderate impact of the 2015 El Niño over East Africa and its representation in
493 seasonal reforecasts. *Journal of Climate*, 32(22), 7989-8001. <https://doi.org/10.1175/JCLI-D-19-0201.1>

494 MacLeod, D., Graham, R., O'Reilly, C., Otieno, G., & Todd, M. (2021). Causal pathways linking different flavours of ENSO
495 with the Greater Horn of Africa short rains. *Atmospheric Science Letters*, 22(2), e1015.
496 <https://doi.org/https://doi.org/10.1002/asl.1015>

497 MacQueen, J. (1967). *Some methods for classification and analysis of multivariate observations*. Paper presented at the Proceedings of
498 the fifth Berkeley symposium on mathematical statistics and probability.

- 499 McKenna, S., Santoso, A., Gupta, A. S., Taschetto, A. S., & Cai, W. (2020). Indian Ocean Dipole in CMIP5 and CMIP6:
500 characteristics, biases, and links to ENSO. *Scientific Reports*, 10(1), 11500. <https://doi.org/10.1038/s41598-020-68268-9>
- 501 Mwangi, E., Wetterhall, F., Dutra, E., Di Giuseppe, F., & Pappenberger, F. (2014). Forecasting droughts in East Africa. *Hydrol.*
502 *Earth Syst. Sci.*, 18(2), 611-620. <https://doi.org/10.5194/hess-18-611-2014>
- 503 Nicholson, S. E. (2015). Long-term variability of the East African ‘short rains’ and its links to large-scale factors. *International*
504 *Journal of Climatology*, 35(13), 3979-3990. <https://doi.org/10.1002/joc.4259>
- 505 Nicholson, S. E. (2017). Climate and climatic variability of rainfall over eastern Africa. *Reviews of Geophysics*, 55, 590–635.
506 <https://doi.org/10.1002/2016RG000544>
- 507 Nyamekye, A. B., Nyadzi, E., Dewulf, A., Werners, S., Van Slobbe, E., Biesbroek, R. G., . . . Ludwig, F. (2021). Forecast
508 probability, lead time and farmer decision-making in rice farming systems in Northern Ghana. *Climate Risk*
509 *Management*, 31, 100258. <https://doi.org/https://doi.org/10.1016/j.crm.2020.100258>
- 510 Nyenzi, B. S. (1988). *Mechanisms of East African rainfall variability*. (Ph.D. thesis), The Florida State University. (8814426)
- 511 Ropelewski, C. F., & Halpert, M. S. (1987). Global and Regional Scale Precipitation Patterns Associated with the El
512 Niño/Southern Oscillation. *Monthly Weather Review*, 115(8), 1606-1626. [https://doi.org/10.1175/1520-0493\(1987\)115<1606:GARSPP>2.0.CO;2](https://doi.org/10.1175/1520-0493(1987)115<1606:GARSPP>2.0.CO;2)
- 513
- 514 Saji, N. H., Goswami, B. N., Vinayachandran, P. N., & Yamagata, T. (1999). A dipole mode in the tropical Indian Ocean.
515 *Nature*, 401(6751), 360-363. <https://doi.org/10.1038/43854>
- 516 Schreck, C. J. I., & Semazzi, F. H. M. (2004). Variability of the recent climate of eastern Africa. *International Journal of*
517 *Climatology*, 24(6), 681-701. <https://doi.org/https://doi.org/10.1002/joc.1019>
- 518 Stuecker, M. F., Timmermann, A., Jin, F.-F., Chikamoto, Y., Zhang, W., Wittenberg, A. T., . . . Zhao, S. (2017). Revisiting
519 ENSO/Indian Ocean Dipole phase relationships. *Geophysical Research Letters*, 44(5), 2481-2492.
520 <https://doi.org/https://doi.org/10.1002/2016GL072308>
- 521 Tall, A., Coulibaly, J. Y., & Diop, M. (2018). Do climate services make a difference? A review of evaluation methodologies and
522 practices to assess the value of climate information services for farmers: Implications for Africa. *Climate Services*, 11, 1-
523 12. <https://doi.org/https://doi.org/10.1016/j.cliser.2018.06.001>
- 524 Ummerhofer, C. C., Sen Gupta, A., England, M. H., & Reason, C. J. (2009). Contributions of Indian Ocean sea surface
525 temperatures to enhanced East African rainfall. *Journal of Climate*, 22(4), 993-1013.
526 <https://doi.org/10.1175/2008JCLI2493.1>
- 527 Vigaud, N., Lyon, B., & Giannini, A. (2017). Sub-seasonal teleconnections between convection over the Indian Ocean, the East
528 African long rains and tropical Pacific surface temperatures. *International Journal of Climatology*, 37(3), 1167-1180.
529 <https://doi.org/https://doi.org/10.1002/joc.4765>
- 530 Wainwright, C. M., Finney, D. L., Kilavi, M., Black, E., & Marsham, J. H. (2021). Extreme rainfall in East Africa, October
531 2019–January 2020 and context under future climate change. *Weather*, 76(1), 26-31.
532 <https://doi.org/https://doi.org/10.1002/wea.3824>
- 533 Walker, D. P., Birch, C. E., Marsham, J. H., Scaife, A. A., Graham, R. J., & Segele, Z. T. J. C. D. (2019). Skill of dynamical and
534 GHACOF consensus seasonal forecasts of East African rainfall. <https://doi.org/10.1007/s00382-019-04835-9>
- 535 Wenhaji Ndomeni, C., Cattani, E., Merino, A., & Levizzani, V. (2018). An observational study of the variability of East African
536 rainfall with respect to sea surface temperature and soil moisture. *Quarterly Journal of the Royal Meteorological Society*,
537 144(S1), 384-404. <https://doi.org/https://doi.org/10.1002/qj.3255>
- 538 Zhao, S., & Cook, K. H. (2021). Influence of Walker circulations on East African rainfall. *Climate Dynamics*, 56, 2127–2147.
539 <https://doi.org/10.1007/s00382-020-05579-7>
- 540 Zheng, X.-T., Lu, J., & Hui, C. (2021). Response of seasonal phase locking of Indian Ocean Dipole to global warming. *Climate*
541 *Dynamics*. <https://doi.org/10.1007/s00382-021-05834-5>

542

543